Available online at www.sciencedirect.com
SCIENCE DIRECT
International Journal of Heat and Mass Transfer 49 (2006) 4525–4535
International Journal of HEAT and MASS TRANSFER
www.elsevier.com/locate/ijhmt

Effects of thermal boundary conditions on natural convection flows within a square cavity

Tanmay Basak [a], S. Roy [b], A.R. Balakrishnan [a,*]

[a] Department of Chemical Engineering, Indian Institute of Technology Madras, Chennai 600 036, India
[b] Department of Mathematics, Indian Institute of Technology Madras, Chennai 600 036, India

Received 13 January 2006
Available online 25 July 2006

Abstract

A numerical study to investigate the steady laminar natural convection flow in a square cavity with uniformly and non-uniformly heated bottom wall, and adiabatic top wall maintaining constant temperature of cold vertical walls has been performed. A penalty finite element method with bi-quadratic rectangular elements has been used to solve the governing mass, momentum and energy equations. The numerical procedure adopted in the present study yields consistent performance over a wide range of parameters (Rayleigh number Ra, $10^3 \leqslant Ra \leqslant 10^5$ and Prandtl number Pr, $0.7 \leqslant Pr \leqslant 10$) with respect to continuous and discontinuous Dirichlet boundary conditions. Non-uniform heating of the bottom wall produces greater heat transfer rates at the center of the bottom wall than the uniform heating case for all Rayleigh numbers; however, average Nusselt numbers show overall lower heat transfer rates for the non-uniform heating case. Critical Rayleigh numbers for conduction dominant heat transfer cases have been obtained and for convection dominated regimes, power law correlations between average Nusselt number and Rayleigh numbers are presented.

Keywords: Penalty finite element method; Natural convection; Square cavity; Uniform and non-uniform heating

1. Introduction

Natural convection in a closed square cavity has occupied the center stage in many fundamental heat transfer analysis which is of prime importance in certain technological applications. In fact, buoyancy-driven convection in a sealed cavity with differentially heated isothermal walls is a prototype of many industrial application such as energy efficient design of buildings and rooms, operation and safety of nuclear reactors and convective heat transfer associated with boilers. Buoyancy driven flows are complex because of essential coupling between the transport properties of flow and thermal fields. In particular, internal flow problems are considerably more complex than external ones. This is because at large Rayleigh number (product of Prandtl and Grashof numbers) classical boundary layer theory can assume the simplifications for external flow problems, namely, the region outside the boundary layer is unaffected by the boundary layer. For confined natural convection, in contrast, boundary layers form near the walls but the region external to them is enclosed by the boundary layers and forms a core region. Since the core is partially or fully encircled by the boundary layers, the core flow is not readily determined from the boundary conditions but depend on the boundary layer, which, in turn, is influenced by the core. The interactions between the boundary layer and core constitute a major complexity in the problem. In fact, the situation is even more intricate because it often appears that more than one global core flow is possible and flow subregions, such as, cells and layers, may be embedded in the core. A literature survey shows that the comprehensive review of these problems was made by Ostrach [1–3], Gebhart [4] and Hoogendoorn

* Corresponding author. Tel.: +91 44 2257 4154; fax: +91 44 2257 0509.
E-mail addresses: tanmay@iitm.ac.in (T. Basak), sjroy@iitm.ac.in (S. Roy), arbala@iitm.ac.in (A.R. Balakrishnan).

0017-9310/$ - see front matter © 2006 Elsevier Ltd. All rights reserved.
doi:10.1016/j.ijheatmasstransfer.2006.05.015

Nomenclature

g	acceleration due to gravity (m s^{-2})
J	Jacobian of residual equations
k	thermal conductivity (W m^{-1} K^{-1})
L	side of the square cavity (m)
N	total number of nodes
Nu	local Nusselt number
p	pressure (Pa)
P	dimensionless pressure
Pr	Prandtl number
R	residual of weak form
Ra	Rayleigh number
T	temperature (K)
T_h	temperature of hot bottom wall (K)
T_c	temperature of cold vertical wall (K)
u	x component of velocity
U	x component of dimensionless velocity
v	y component of velocity
V	y component of dimensionless velocity
X	dimensionless distance along x coordinate
Y	dimensionless distance along y coordinate

Greek symbols

α	thermal diffusivity (m^2 s^{-1})
β	volume expansion coefficient (K^{-1})
γ	penalty parameter
θ	dimensionless temperature
ν	kinematic viscosity (m^2 s^{-1})
ρ	density (kg m^{-3})
Φ	basis functions
ψ	stream function
ξ	horizontal coordinate in a unit square
η	vertical coordinate in a unit square

Subscripts

b	bottom wall
i	residual number
k	node number
s	side wall

Superscript

n	Newton iterative index

[5] in which each emphasizes essentially various aspects of the subject.

Perusal of prior numerical investigations by Patterson and Imberger [6], Nicolette et al. [7], Hall et al. [8], Hyun and Lee [9], Fusegi et al. [10], Lage and Bejan [11,12], and Xia and Murthy [13] reveal that several attempts have been made to acquire a basic understanding of natural convection flows and heat transfer characteristics in an enclosure. However, in most of these studies, one vertical wall of the enclosure is cooled and another one heated while the remaining top and bottom walls are well insulated. November and Nansteel [14] and Valencia and Frederick [15] have shown a specific interest to focus on a natural convection within a rectangular enclosure wherein a bottom heating and/or a top cooling are involved. Studies on natural convection in rectangular enclosures heated from below and cooled along a single side or both sides have been carried out by Ganzarolli and Milanez [16]. Later, the case of heating from one side and cooling from the top has been analyzed by Aydin et al. [17] who investigated the influence of aspect ratio for air-filled rectangular enclosures. Also, Kirkpatrick and Bohn [18] examined experimentally the case of high Rayleigh number natural convection in a water-filled cubical enclosure heated simultaneously from below and from the side. Recently, Corcione [19] has studied natural convection in a air-filled rectangular enclosure heated from below and cooled from above for a variety of thermal boundary conditions at the side walls. Numerical results were reported for several values of both width-to-height aspect ratio of the enclosure and Rayleigh number.

The aim of the present study is to investigate natural convection in a square cavity when bottom wall is heated (uniformly and non-uniformly) and top wall is well insulated while two vertical walls are cooled by means of two constant temperature baths (see Fig. 1). In case of uniformly heated bottom wall, the finite discontinuities in temperature distribution appear at the edges of the bottom wall. The discontinuities can be avoided by choosing a non-uniform temperature distribution along the bottom

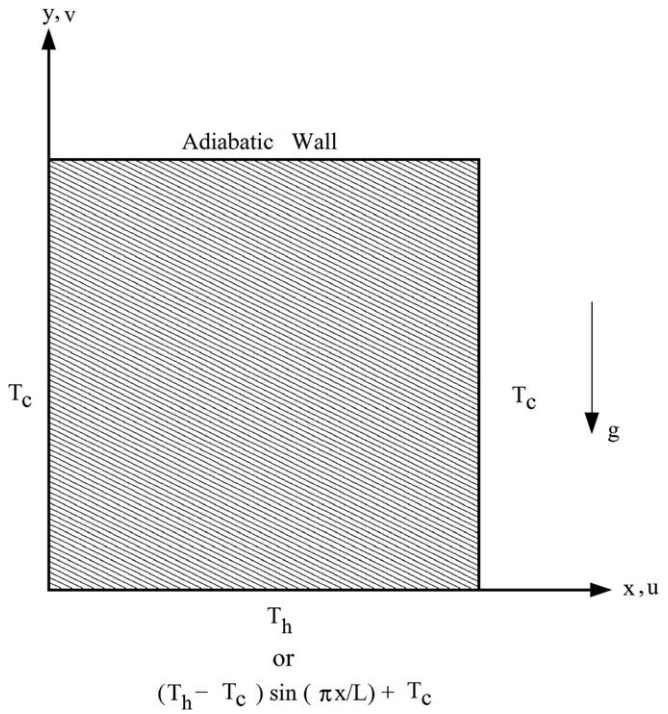

Fig. 1. Schematic diagram of the physical system.

wall (i.e., non-uniformly heated bottom wall) as discussed by Minkowycz et al. [20] where an investigation is made for a mixed convection flow on a vertical plate, which is either heated or cooled. In the current study, we have used Galerkin finite element method with penalty parameter to solve the non-linear coupled partial differential equations of flow and temperature fields for both uniform and non-uniform temperature distribution prescribed at the bottom wall. The results will be illustrated for $Ra = 10^3$–10^5 with $Pr = 0.7$–10 to represent influence of natural convection on heat transfer rates in terms of local and average Nusselt numbers at the bottom and side walls.

2. Mathematical formulation

The flow model is based on the assumptions that the fluid is Newtonian and that the properties are constant with the exception of the density in the body force term of the momentum equation. The Boussinesq approximation is invoked for the fluid properties to relate density changes to temperature changes, and so to couple in this way the temperature field to the flow field. The governing equations for natural convection flow using conservation of mass, momentum and energy can be written as:

$$\frac{\partial u}{\partial x}+\frac{\partial v}{\partial y}=0 \tag{1}$$

$$u\frac{\partial u}{\partial x}+v\frac{\partial u}{\partial y}=-\frac{1}{\rho}\frac{\partial p}{\partial x}+\nu\left(\frac{\partial^2 u}{\partial x^2}+\frac{\partial^2 u}{\partial y^2}\right) \tag{2}$$

$$u\frac{\partial v}{\partial x}+v\frac{\partial v}{\partial y}=-\frac{1}{\rho}\frac{\partial p}{\partial y}+\nu\left(\frac{\partial^2 v}{\partial x^2}+\frac{\partial^2 v}{\partial y^2}\right)+g\beta(T-T_c) \tag{3}$$

$$u\frac{\partial T}{\partial x}+v\frac{\partial T}{\partial y}=\alpha\left(\frac{\partial^2 T}{\partial x^2}+\frac{\partial^2 T}{\partial y^2}\right) \tag{4}$$

with boundary conditions

$$\begin{aligned}&u(x,0)=u(x,L)=u(0,y)=u(L,y)=0\\&v(x,0)=v(x,L)=v(0,y)=v(L,y)=0\\&T(x,0)=T_h \quad \text{or} \quad T(x,0)=(T_h-T_c)\sin\left(\frac{\pi x}{L}\right)+T_c\\&\frac{\partial T}{\partial y}(x,L)=0, \quad T(0,y)=T(L,y)=T_c\end{aligned} \tag{5}$$

where x and y are the distances measured along the horizontal and vertical directions, respectively; u and v are the velocity components in the x- and y-directions, respectively; T denotes the temperature; ν and α are kinematic viscosity and thermal diffusivity, respectively; p is the pressure and ρ is the density; T_h and T_c are the temperatures at hot bottom wall and cold vertical walls, respectively; L is the side of the square cavity.

Using the following change of variables:

$$\begin{aligned}&X=\frac{x}{L}, \quad Y=\frac{y}{L}, \quad U=\frac{uL}{\alpha}, \quad V=\frac{vL}{\alpha}, \quad \theta=\frac{T-T_c}{T_h-T_c},\\&P=\frac{pL^2}{\rho\alpha^2}, \quad Pr=\frac{\nu}{\alpha}, \quad Ra=\frac{g\beta(T_h-T_c)L^3Pr}{\nu^2}\end{aligned} \tag{6}$$

the governing equations (1)–(4) reduce to non-dimensional form:

$$\frac{\partial U}{\partial X}+\frac{\partial V}{\partial Y}=0 \tag{7}$$

$$U\frac{\partial U}{\partial X}+V\frac{\partial U}{\partial Y}=-\frac{\partial P}{\partial X}+Pr\left(\frac{\partial^2 U}{\partial X^2}+\frac{\partial^2 U}{\partial Y^2}\right) \tag{8}$$

$$U\frac{\partial V}{\partial X}+V\frac{\partial V}{\partial Y}=-\frac{\partial P}{\partial Y}+Pr\left(\frac{\partial^2 V}{\partial X^2}+\frac{\partial^2 V}{\partial Y^2}\right)+Ra\,Pr\theta \tag{9}$$

$$U\frac{\partial \theta}{\partial X}+V\frac{\partial \theta}{\partial Y}=\frac{\partial^2 \theta}{\partial X^2}+\frac{\partial^2 \theta}{\partial Y^2} \tag{10}$$

with boundary conditions

$$\begin{aligned}&U(X,0)=U(X,1)=U(0,Y)=U(1,Y)=0\\&V(X,0)=V(X,1)=V(0,Y)=V(1,Y)=0\\&\theta(X,0)=1 \quad \text{or} \quad \theta(X,0)=\sin(\pi X)\\&\theta(0,Y)=\theta(1,Y)=0, \quad \frac{\partial\theta}{\partial Y}(X,1)=0\end{aligned} \tag{11}$$

Here X and Y are dimensionless coordinates along horizontal and vertical directions, respectively; U and V are, dimensionless velocity components in the X- and Y-directions, respectively; θ is the dimensionless temperature; P is the dimensionless pressure; Ra and Pr are Rayleigh and Prandtl numbers, respectively.

3. Solution procedure

The momentum and energy balance equations (8)–(10) are solved using the Galerkin finite element method. The continuity equation (7) will be used as a constraint due to mass conservation and this constraint may be used to obtain the pressure distribution (Basak and Ayappa [21]; Reddy [22]). In order to solve equations (8)–(10), we use the penalty finite element method where the pressure P is eliminated by a penalty parameter γ and the incompressibility criteria given by Eq. (7) (see Reddy [22]) which results in:

$$P=-\gamma\left(\frac{\partial U}{\partial X}+\frac{\partial V}{\partial Y}\right). \tag{12}$$

The continuity equations (7) is automatically satisfied for large values of γ. Typical values of γ that yield consistent solutions are 10^7 (Basak and Ayappa [21]; Reddy [22]).

Using Eq. (12), the momentum balance equations (8) and (9) reduce to:

$$U\frac{\partial U}{\partial X}+V\frac{\partial U}{\partial Y}=\gamma\frac{\partial}{\partial X}\left(\frac{\partial U}{\partial X}+\frac{\partial V}{\partial Y}\right)+Pr\left(\frac{\partial^2 U}{\partial X^2}+\frac{\partial^2 U}{\partial Y^2}\right) \tag{13}$$

and

$$U\frac{\partial V}{\partial X}+V\frac{\partial V}{\partial Y}=\gamma\frac{\partial}{\partial Y}\left(\frac{\partial U}{\partial X}+\frac{\partial V}{\partial Y}\right)+Pr\left(\frac{\partial^2 V}{\partial X^2}+\frac{\partial^2 V}{\partial Y^2}\right)+RaPr\theta. \tag{14}$$

Expanding the velocity components (U, V) and temperature (θ) using basis set $\{\Phi_k\}_{k=1}^{N}$ as,

$$U \approx \sum_{k=1}^{N} U_k \Phi_k(X,Y), \quad V \approx \sum_{k=1}^{N} V_k \Phi_k(X,Y),$$
$$\text{and} \quad \theta \approx \sum_{k=1}^{N} \theta_k \Phi_k(X,Y), \tag{15}$$
$$\text{for } 0 \leqslant X,\ Y \leqslant 1,$$

the Galerkin finite element method yields the following nonlinear residual equations for Eqs. (13), (14) and (10), respectively, at nodes of internal domain Ω:

$$R_i^{(1)} = \sum_{k=1}^{N} U_k \int_\Omega \left[\left(\sum_{k=1}^{N} U_k \Phi_k \right) \frac{\partial \Phi_k}{\partial X} + \left(\sum_{k=1}^{N} V_k \Phi_k \right) \frac{\partial \Phi_k}{\partial Y} \right] \Phi_i \mathrm{d}X\mathrm{d}Y + \gamma \left[\sum_{k=1}^{N} U_k \int_\Omega \frac{\partial \Phi_i}{\partial X} \frac{\partial \Phi_k}{\partial X} \mathrm{d}X\mathrm{d}Y + \sum_{k=1}^{N} V_k \int_\Omega \frac{\partial \Phi_i}{\partial X} \frac{\partial \Phi_k}{\partial Y} \mathrm{d}X\mathrm{d}Y \right] + Pr \sum_{k=1}^{N} U_k \int_\Omega \left[\frac{\partial \Phi_i}{\partial X} \frac{\partial \Phi_k}{\partial X} + \frac{\partial \Phi_i}{\partial Y} \frac{\partial \Phi_k}{\partial Y} \right] \mathrm{d}X\mathrm{d}Y \tag{16}$$

$$R_i^{(2)} = \sum_{k=1}^{N} V_k \int_\Omega \left[\left(\sum_{k=1}^{N} U_k \Phi_k \right) \frac{\partial \Phi_k}{\partial X} + \left(\sum_{k=1}^{N} V_k \Phi_k \right) \frac{\partial \Phi_k}{\partial Y} \right] \Phi_i \mathrm{d}X\mathrm{d}Y + \gamma \left[\sum_{k=1}^{N} U_k \int_\Omega \frac{\partial \Phi_i}{\partial Y} \frac{\partial \Phi_k}{\partial X} \mathrm{d}X\mathrm{d}Y + \sum_{k=1}^{N} V_k \int_\Omega \frac{\partial \Phi_i}{\partial Y} \frac{\partial \Phi_k}{\partial Y} \mathrm{d}X\mathrm{d}Y \right] + Pr \sum_{k=1}^{N} V_k \int_\Omega \left[\frac{\partial \Phi_i}{\partial X} \frac{\partial \Phi_k}{\partial X} + \frac{\partial \Phi_i}{\partial Y} \frac{\partial \Phi_k}{\partial Y} \right] \mathrm{d}X\mathrm{d}Y - RaPr \int_\Omega \left(\sum_{k=1}^{N} \theta_k \Phi_k \right) \Phi_i \mathrm{d}X\mathrm{d}Y \tag{17}$$

and

$$R_i^{(3)} = \sum_{k=1}^{N} \theta_k \int_\Omega \left[\left(\sum_{k=1}^{N} U_k \Phi_k \right) \frac{\partial \Phi_k}{\partial X} + \left(\sum_{k=1}^{N} V_k \Phi_k \right) \frac{\partial \Phi_k}{\partial Y} \right] \Phi_i \mathrm{d}X\mathrm{d}Y + \sum_{k=1}^{N} \theta_k \int_\Omega \left[\frac{\partial \Phi_i}{\partial X} \frac{\partial \Phi_k}{\partial X} + \frac{\partial \Phi_i}{\partial Y} \frac{\partial \Phi_k}{\partial Y} \right] \mathrm{d}X\mathrm{d}Y \tag{18}$$

Bi-quadratic basis functions with three point Gaussian quadrature is used to evaluate the integrals in the residual equations. In Eqs. (16) and (17), the second term containing the penalty parameter (γ) are evaluated with two point Gaussian quadrature (reduced integration penalty formulation, Reddy [22]). The motivation for reduced integration is given below. The matrix vector notation for the penalty finite element equations of the residuals, i.e., Eqs. (16)–(18) may be expressed in matrix vector notation as:

$$(\mathbf{K_1} + \gamma \mathbf{K_2})\mathbf{a} = \mathbf{F}, \tag{19}$$

where $\mathbf{a}$ denotes the unknown vector, $\mathbf{K}_1$, $\mathbf{K}_2$ are the matrices obtained from the Jacobian of the residuals. As γ tends to a large value ($\sim 10^7$), the constraint equation (i.e., continuity equation) is satisfied better, which in turn causes the magnitude of $\mathbf{K}_1$ to be negligible when compared with $\gamma \mathbf{K}_2$ resulting in:

$$\mathbf{K_2 a} = \frac{\mathbf{F}}{\gamma}. \tag{20}$$

This implies that as γ tends to infinity, the governing equations are left with only the constraint condition, i.e., the continuity equation. Hence, the contributions from the momentum and energy conservations are completely lost. In addition, as $\mathbf{K}_2$ is nonsingular for large γ the resulting solution obtained from Eq. (20) is trivial. To obtain the non-trivial solutions for large $\gamma(\sim 10^7)$ the matrix $\mathbf{K}_2$ needs to be a singular matrix. This is obtained by using two point Gaussian quadrature for $\mathbf{K}_2$ and three point Gaussian quadrature for $\mathbf{K}_1$. In the absence of the above reduced integration method velocities are underestimated (Reddy [22]).

The non-linear residual Eqs. (16)–(18) are solved using a Newton–Raphson procedure to determine the coefficients of the expansions in Eq. (15). At each iteration, the linear $(3N \times 3N)$ system:

$$\mathbf{J}(\mathbf{a}^n)[\mathbf{a}^n - \mathbf{a}^{n+1}] = \mathbf{R}(\mathbf{a}^n) \tag{21}$$

is solved where n is the iterative index. The elements of the Jacobian matrix, $\mathbf{J}(\mathbf{a}^n)$ contains the derivatives of the residual equations with respect to velocity components (U_j)'s, (V_j)'s and the temperature (θ_j)'s and $\mathbf{R}(\mathbf{a}^n)$ is the vector of residuals. The linear system for each iteration is based on efficient node numbering of the elements such that the jacobian forms a banded matrix. The iterative process is terminated with the convergence criterion $\left[\sum (R_i^{(j)})^2\right]^{0.5} \leqslant 10^{-5}$ using two-norm of residual vectors.

A nine node bi-quadratic elements with each element mapped using iso-parametric mapping (Reddy [22]) from $X - Y$ to a unit square $\xi - \eta$ domain has been used. Subsequently, the domain integrals in the residual equations are evaluated using nine node bi-quadratic basis functions in $\xi - \eta$ domain as:

$$X = \sum_{i=1}^{9} X_i \Phi_i(\xi,\eta) \quad \text{and} \quad Y = \sum_{i=1}^{9} Y_i \Phi_i(\xi,\eta), \tag{22}$$

where $\Phi_i(\xi,\eta)$ are the local bi-quadratic basis functions on the $\xi - \eta$ domain. The integrals in Eqs. (16)–(18) can be evaluated in $\xi - \eta$ domain using following relationships:

$$\begin{bmatrix} \frac{\partial \Phi_i}{\partial X} \\ \frac{\partial \Phi_i}{\partial Y} \end{bmatrix} = \frac{1}{J} \begin{bmatrix} \frac{\partial Y}{\partial \eta} & -\frac{\partial Y}{\partial \xi} \\ -\frac{\partial X}{\partial \eta} & \frac{\partial X}{\partial \xi} \end{bmatrix} \begin{bmatrix} \frac{\partial \Phi_i}{\partial \xi} \\ \frac{\partial \Phi_i}{\partial \eta} \end{bmatrix}$$

and

$$\mathrm{d}X\,\mathrm{d}Y = J\mathrm{d}\xi\,\mathrm{d}\eta \tag{23}$$

where

$$J = \frac{\partial(X,Y)}{\partial(\xi,\eta)} = \begin{vmatrix} \frac{\partial X}{\partial \xi} & \frac{\partial X}{\partial \eta} \\ \frac{\partial Y}{\partial \xi} & \frac{\partial Y}{\partial \eta} \end{vmatrix}.$$

4. Evaluation of stream function and Nusselt number

4.1. Stream function

The fluid motion is displayed using the stream function ψ obtained from velocity components U and V. The relationships between stream function, ψ (Batchelor [23]) and velocity components for two dimensional flows are:

$$U = \frac{\partial \psi}{\partial Y} \quad \text{and} \quad V = -\frac{\partial \psi}{\partial X}, \tag{24}$$

which yield a single equation

$$\frac{\partial^2 \psi}{\partial X^2} + \frac{\partial^2 \psi}{\partial Y^2} = \frac{\partial U}{\partial Y} - \frac{\partial V}{\partial X}. \tag{25}$$

Using the above definition of the stream function, the positive sign of ψ denotes anti-clockwise circulation and the clockwise circulation is represented by the negative sign of ψ. Expanding the stream function (ψ) using the basis set $\{\Phi\}$ as $\psi = \sum_{k=1}^{N} \psi_k \Phi_k(X,Y)$ and the relation for U and V from Eq. (15), the Galerkin finite element method yields the following linear residual equations for Eq. (25).

$$R_i^s = \sum_{k=1}^{N} \psi_k \int_\Omega \left[\frac{\partial \Phi_i}{\partial X}\frac{\partial \Phi_k}{\partial X} + \frac{\partial \Phi_i}{\partial Y}\frac{\partial \Phi_k}{\partial Y} \right] \mathrm{d}X\mathrm{d}Y + \sum_{k=1}^{N} U_k \int_\Omega \Phi_i \frac{\partial \Phi_k}{\partial Y} \mathrm{d}X\mathrm{d}Y - \sum_{k=1}^{N} V_k \int_\Omega \Phi_i \frac{\partial \Phi_k}{\partial X} \mathrm{d}X\mathrm{d}Y \tag{26}$$

The no-slip condition is valid at all boundaries as there is no cross flow, hence $\psi = 0$ is used as residual equations at the nodes for the boundaries. The bi-quadratic basis function is used to evaluate the integrals in Eq. (26) and ψ's are obtained by solving the N linear residual equation (26).

4.2. Nusselt number

The heat transfer coefficient in terms of the local Nusselt number (Nu) is defined by:

$$Nu = -\frac{\partial \theta}{\partial n}, \tag{27}$$

where n denotes the normal direction on a plane. The normal derivative is evaluated by the bi-quadratics basis set in $\xi - \eta$ domain using Eqs. (22) and (23). The local Nusselt numbers at the bottom wall (Nu_b) and at the side wall (Nu_s) are defined as:

$$Nu_\mathrm{b} = -\sum_{i=1}^{9} \theta_i \frac{\partial \Phi_i}{\partial Y} \tag{28}$$

and

$$Nu_\mathrm{s} = -\sum_{i=1}^{9} \theta_i \frac{\partial \Phi_i}{\partial X}. \tag{29}$$

The average Nusselt numbers at the bottom and side walls are:

$$\overline{Nu_\mathrm{b}} = \frac{\int_0^1 Nu_\mathrm{b}\mathrm{d}X}{X|_0^1} = \int_0^1 Nu_\mathrm{b}\mathrm{d}X \tag{30}$$

and

$$\overline{Nu_\mathrm{s}} = \frac{\int_0^1 Nu_\mathrm{s}\mathrm{d}Y}{Y|_0^1} = \int_0^1 Nu_\mathrm{s}\mathrm{d}Y. \tag{31}$$

5. Results and discussion

5.1. Numerical tests

The computational domain consists of 20×20 bi-quadratic elements which correspond to 41×41 grid points. The bi-quadratic elements with lesser number of nodes smoothly capture the non-linear variations of the field variables which are in contrast with finite difference/finite volume solutions available in the literature [10–12]. In order to assess the accuracy of the numerical procedure, the algorithm based on the grid size (41×41) for a square enclosure with a side wall heated were compared and are in agreement with the work of Mallinson and Vahl Davis [24] for $Ra = 10^3$–10^6. Comparisons are not shown in this paper.

Computations have been carried out for various values of $Ra = 10^3$–10^5 and $Pr = 0.7$–10 with uniform and non-uniform bottom wall heating where side walls are cooled and the top wall is well insulated. The jump discontinuities in Dirichlet type wall boundary conditions at the corner points (see Fig. 1) correspond to computational singularities. In particular, the singularity at the corner nodes of the bottom wall needs special attention. The grid size dependent effect of the temperature discontinuity at the corner points on the local (and the overall) Nusselt numbers tend to increase as the mesh spacing at the corner is reduced. One way for handling the problem is assuming the average temperature of the two walls at the corner and keeping the adjacent grid-nodes at the respective wall temperatures as suggested by Ganzarolli and Milanez [16]. This procedure is still grid dependent unless a sufficiently refined mesh is implemented. Once any corner formed by the intersection of two differently heated boundary walls is assumed at the average temperature of the adjacent walls, the optimal grid size obtained for each configuration corresponds to the mesh spacing over which further grid refinements lead to grid invariant results in both heat transfer rates and flow fields. Similar observations were also reported by Corcione [19].

In the current investigation, Gaussian quadrature based finite element method provides smooth solutions in the

computational domain including the corner regions as evaluation of residuals depends on interior gauss points and thus the effect of corner nodes are less pronounced in the final solution. In general, the Nusselt numbers for finite difference/finite volume based methods are calculated at any surface using some interpolation functions which are avoided in the current work. The present finite element approach offers special advantage on evaluation of local Nusselt number at the bottom and side walls as the element basis functions are used to evaluate the heat flux. It may be noted that the number of grid points in the current study is 41×41 and these nodal numbers are in agreement with the number of grid points of 33×33 as illustrated by Corcione [19]. In addition, the percent changes of the average Nusselt numbers ($\overline{Nu_b}$ and $\overline{Nu_s}$) and the maximum horizontal and vertical dimensionless velocity components at an assigned vertical and horizontal plane across the cavity are within 0.1–1%.

5.2. Effects of Rayleigh number: uniform heating at bottom wall

Figs. 2–5 illustrate the stream function and isotherm contours of the numerical results for various $Ra = 10^3$–10^5 and $Pr = 0.7$–10 when the bottom wall is uniformly heated. As expected, due to the cold vertical walls, fluids rise up from middle portion of the bottom wall and flow down along the two vertical walls forming two symmetric rolls with clockwise and anti-clockwise rotations inside the cavity. At $Ra = 10^3$, the magnitudes of stream function are very low and the heat transfer is primarily due to conduction. During conduction dominant heat transfer, the temperature contours with $\theta = 0.1$ occur symmetrically near the side walls of the enclosure. The other temperature contours with $\theta \geqslant 0.2$ are smooth curves which span the entire enclosure and they are generally symmetric with respect to the vertical center line. The temperature contours as indicated in Fig. 2 remains invariant up to $Ra < 5 \times 10^3$.

At $Ra = 5 \times 10^3$, the circulation near the central regimes are stronger and consequently, the temperature contour with $\theta = 0.2$ starts getting shifted towards the side wall and they break into two symmetric contour lines (Fig. 3). The presence of significant convection is also exhibited in other temperature contours lines which start getting deformed and pushed towards the top plate.

As Rayleigh number increases to 10^5, the buoyancy driven circulation inside the cavity also increases as seen from the greater magnitudes of the stream functions (Fig. 4). The circulations are greater near the center and least at the wall due to no slip boundary conditions. The greater circulation in each half of the cavity follows a progressive wrapping around the centers of rotation, and a more pronounced compression of the isotherms toward the boundary surfaces of the enclosures occur. Consequently, at $Ra = 10^5$, the temperature gradients near both the bottom and side walls tend to be significant leading to the development of a thermal boundary layer. Due to greater circulations near the central core at the top half of the enclosure, there are small gradients in temperature whereas a large stratification zone of temperature is observed at the vertical symmetry line due to stagnation of flow. Fig. 2 shows that the thermal boundary layer develops even approximately 80% of the cavity for $Ra = 10^3$ whereas for $Ra = 10^5$, the isotherms presented in Fig. 4 indicate that the thermal boundary layer develops almost throughout the entire cavity.

Comparison of Figs. 4 and 5 show that as Pr increases from 0.7 to 10, the values of the stream function and isotherms in the core cavity increase. Although the stream functions look qualitatively similar to that with $Pr = 0.7$, the greater circulation near the central regime of each half distributes greater heat resulting in greater temperature near the central symmetric vertical plane as seen in Fig. 5. It may be noted that the temperature varies within 0.4–0.5 for $Pr = 0.7$ (Fig. 4) near the central core regime at the top half of the enclosure whereas the temperature varies

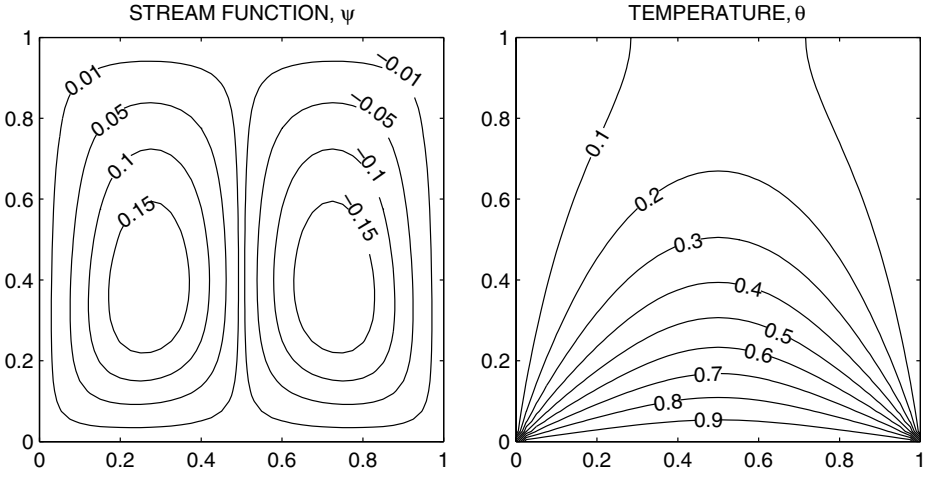

Fig. 2. Contour plots for uniform bottom heating, $\theta(X,0) = 1$, with $Pr = 0.7$ and $Ra = 10^3$. Clockwise and anti-clockwise flows are shown via negative and positive signs of stream functions, respectively.

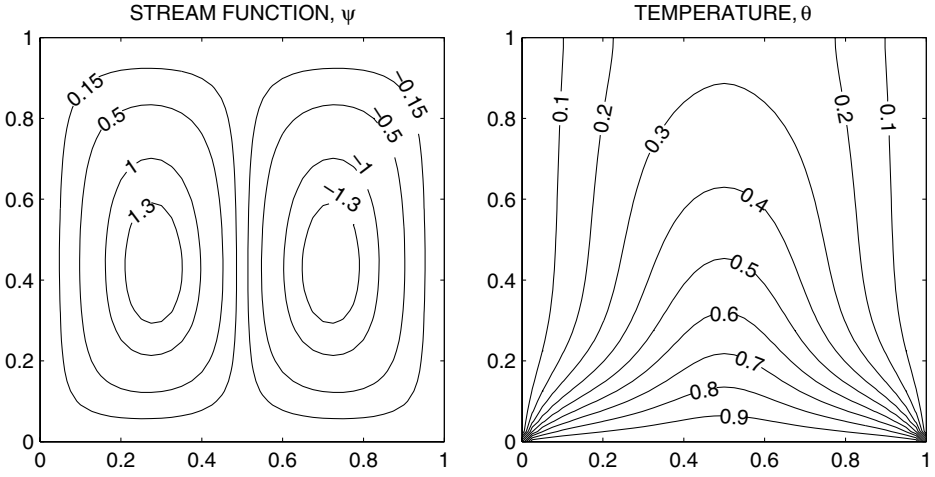

Fig. 3. Contour plots for uniform bottom heating, $\theta(X,0)=1$, with $Pr=0.7$ and $Ra=5\times10^3$. Clockwise and anti-clockwise flows are shown via negative and positive signs of stream functions, respectively.

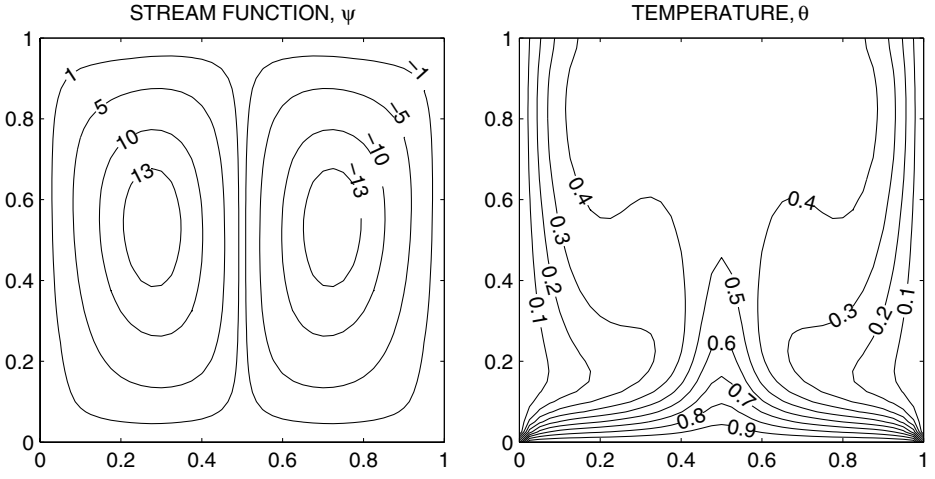

Fig. 4. Contour plots for uniform bottom heating, $\theta(X,0)=1$, with $Pr=0.7$ and $Ra=10^5$. Clockwise and anti-clockwise flows are shown via negative and positive signs of stream functions, respectively.

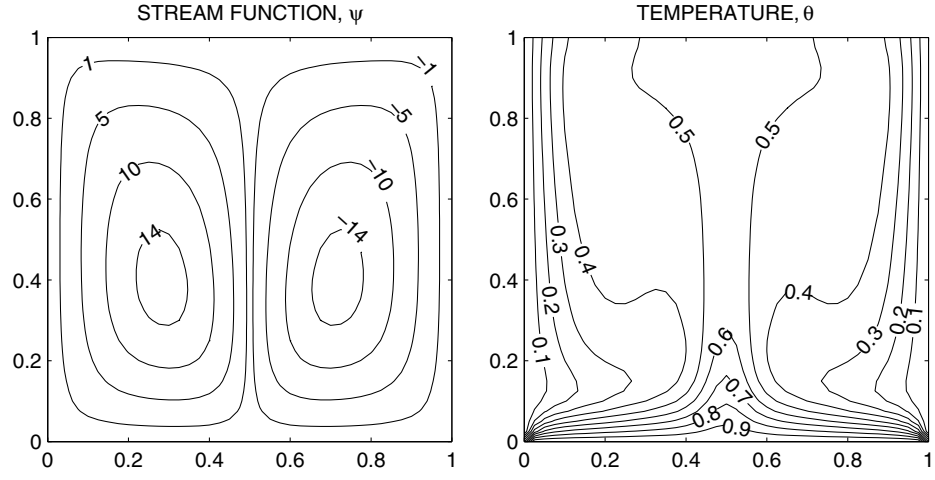

Fig. 5. Contour plots for uniform bottom heating, $\theta(X,0)=1$, with $Pr=10$ and $Ra=10^5$. Clockwise and anti-clockwise flows are shown via negative and positive signs of stream functions, respectively.

within 0.5–0.6 for $Pr = 10$ as seen in Fig. 5. Due to greater circulation at $Pr = 10$, the zone of stratification of temperature at the central symmetric line is reduced.

5.3. Effects of Rayleigh number: non-uniform heating at bottom wall

Stream function contours and isotherms are shown in Figs. 6–8 for $Ra = 10^3$–10^5 and $Pr = 0.7$–10 when the bottom wall is non-uniformly heated. As seen earlier, uniform heating of the bottom wall causes a finite discontinuity in Dirichlet type boundary conditions for the temperature distribution at the edges of the bottom wall. In contrast, the non-uniform heating removes the singularities at the edges of the bottom wall and provides a smooth temperature distribution in the entire cavity. Due to the non-uniform heating of the bottom wall for $Ra = 10^3$ and $Pr = 0.7$, thermal boundary layer develops only over 60% of the cavity (Fig. 6), which is less compared to the uniform heating case. The conduction dominant heat transfer mode is observed up to $Ra = 2 \times 10^4$ which is in contrast with the uniform heating case where the critical Rayleigh number is around 5000. It may be noted that the temperature at the bottom wall is non-uniform and a maxima in temperature occurs at the center. Therefore, greater heat transfer rates occur at the center as illustrated in the next section.

At $Ra = 10^5$, the circulation pattern is qualitatively similar to the uniform heating case (Fig. 7). Due to non-uniform bottom heating, the heating rate near the wall is generally lower which induces less buoyancy resulting in lower thermal gradient throughout the domain. The uniformity in temperature distribution and least temperature gradient are still observed at the central core regime within the top half of the domain. The lower buoyancy effect also leads to a large zone of stratification of temperature at the vertical line of symmetry (Fig. 7). The effect of Prandtl

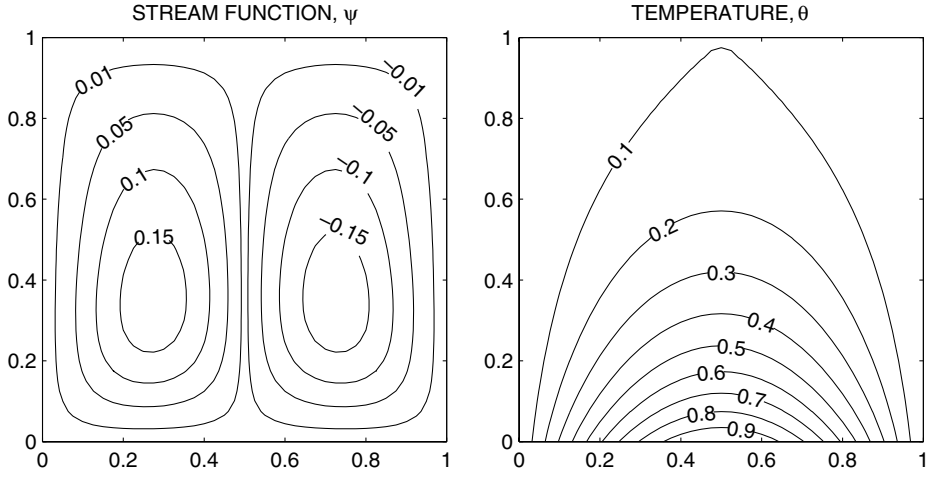

Fig. 6. Contour plots for non-uniform bottom heating, $\theta(X,0) = \sin(\pi X)$, with $Pr = 0.7$ and $Ra = 10^3$. Clockwise and anti-clockwise flows are shown via negative and positive signs of stream functions, respectively.

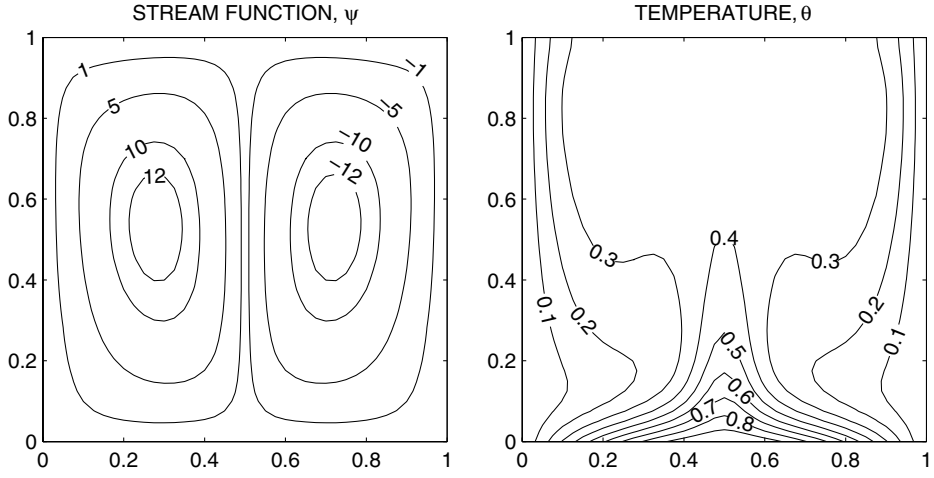

Fig. 7. Contour plots for non-uniform bottom heating, $\theta(X,0) = \sin(\pi X)$, with $Pr = 0.7$ and $Ra = 10^5$. Clockwise and anti-clockwise flows are shown via negative and positive signs of stream functions, respectively.

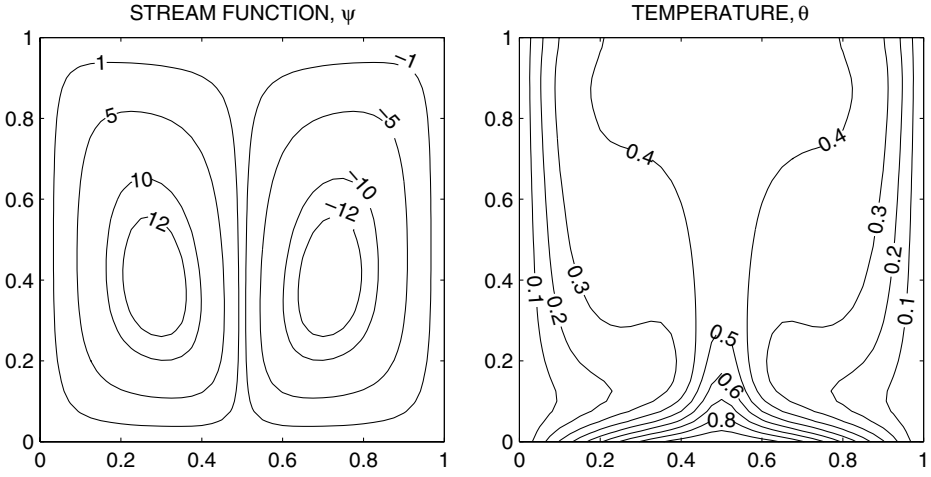

Fig. 8. Contour plots for non-uniform bottom heating, $\theta(X,0) = \sin(\pi X)$, with $Pr = 10$ and $Ra = 10^5$. Clockwise and anti-clockwise flows are shown via negative and positive signs of stream functions, respectively.

number is also pronounced for $Ra = 10^5$ as seen in Fig. 8 where the greater circulation causes more heat to be distributed in the central regime. However, compared to uniform heating cases, the values of temperature contours are lower near the central and top portion of the enclosure for non-uniform heating. The temperature contours are highly dense near the bottom wall which may indicate a lower heating rate at the top as well as central regions of the enclosure.

5.4. Heat transfer rates: local and average Nusselt numbers

Fig. 9 shows the effects of Ra and Pr on the local Nusselt numbers at the bottom and side walls (Nu_b, Nu_s). For uniform heating of the bottom wall, the heat transfer rate or Nu_b is very high at the edges of the bottom wall due to the discontinuities present in the temperature boundary conditions at the edges and reduces towards the center of the bottom wall with the minimum value at the center (Fig. 9(a)). On the contrary, for $Ra = 10^3$ with non-uniformly heated bottom wall, Nu_b increases from zero at both the edges of the bottom wall towards the center with its maximum value at the center. Further, at $Ra = 10^5$, non-uniform heating produces a sinusoidal type of local heat transfer rate with minimum values at the edges as well as at the center of the bottom wall. The physical reason for this type of behavior is due to the higher values of the stream function (i.e., high flow rate) for $Ra = 10^5$ in the middle of the first and second half of the cavity. As Pr increases from 0.7 to 10, the local Nusselt number at the bottom wall (Nu_b) increases slightly as seen in Fig. 9(a). It may be noted that for all values of Prandtl and Rayleigh numbers, non-uniform heating enhances the heat transfer at the central regime only. The temperature contours diverge from the corner points toward the central vertical line for uniform heating and therefore local Nusselt number is a monotonically decreasing function with distance. In contrast, for non-uniform heating the temperature contours are compressed around the intermediate zones between corners and the vertical line of symmetry, and local Nusselt number is maximum at around $X = 0.3$ and 0.7.

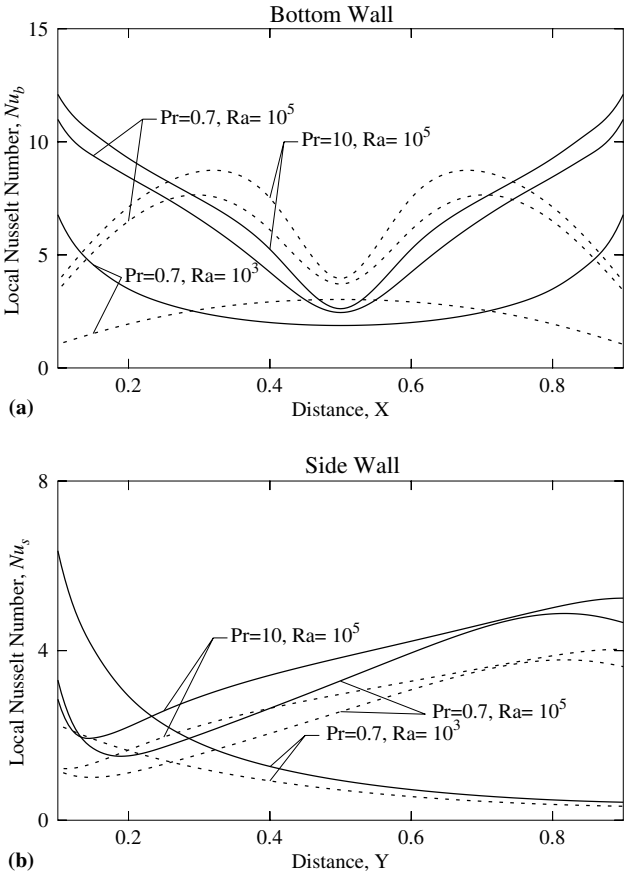

Fig. 9. Variation of local Nusselt number with distance (a) at the bottom wall (b) at the side wall for uniform heating (—) and non-uniform heating (- - -).

Fig. 9(b) illustrates the heat transfer rate at the side wall. The local Nusselt number (Nu_s) decreases with distance at

the side or cold wall for $Ra = 10^3$, $Pr = 0.7$ for both uniform and non-uniform heating. It may be noted that, the heat transfer rate initially decreases and later increases with distance for $Ra = 10^5$ with $Pr = 0.7$ and 10. At higher Rayleigh numbers, the significant circulation as seen in Figs. 4,5,7 and 8 results in highly dense contours at the top portion of the side walls and these dense temperature contours are in contrast with the conduction dominant cases as seen in Figs. 2 and 6. Further, it is observed that the temperature contours are compressed towards the side walls away from the corner points at the bottom. Therefore, the heat fluxes are enhanced at the regions away from bottom corner points. The heat transfer rates are qualitatively similar, but reduced for non-uniform bottom wall heating as compared to uniform heating.

The overall effect on the heat transfer rates are shown in Fig. 10(a)–(d), where the distributions of the average Nusselt number of bottom and side walls, respectively, are plotted versus the logarithmic Rayleigh number. Fig. 10(a) and (b) (cases a and b) illustrate uniform heating and Fig. 10(c) and (d) (cases c and d) illustrate non-uniform heating. For all these cases, it is observed that average Nusselt numbers for both the bottom and side walls remain constant up to $Ra = 5000$ for uniform heating and upto $Ra = 2 \times 10^4$ for non-uniform heating. Hence, dominant heat conduction mode corresponding to a larger range of Rayleigh numbers produces overall lower heat transfer rates for non-uniform heating. The insets show the log–log plot for average Nusselt number versus Rayleigh number for convection dominant regimes. The log–log linear plot is obtained with more than 20 data set. A least square curve is fitted and the overall error is within 1%. The following correlations are obtained for cases a, b, c and d as follows:

Cases a and b: uniform heating ($Ra \geqslant 5000$)

$$\begin{aligned}\overline{Nu_b} &= 2\overline{Nu_s} \\ &= 1.6219Ra^{0.145}, \quad Pr = 0.7 \\ &= 1.2238Ra^{0.177}, \quad Pr = 10\end{aligned} \tag{32}$$

Cases c and d: non-uniform heating ($Ra \geqslant 2 \times 10^4$)

$$\begin{aligned}\overline{Nu_b} &= 2\overline{Nu_s} \\ &= 0.2939Ra^{0.249}, \quad Pr = 0.7 \\ &= 0.2129Ra^{0.289}, \quad Pr = 10\end{aligned} \tag{33}$$

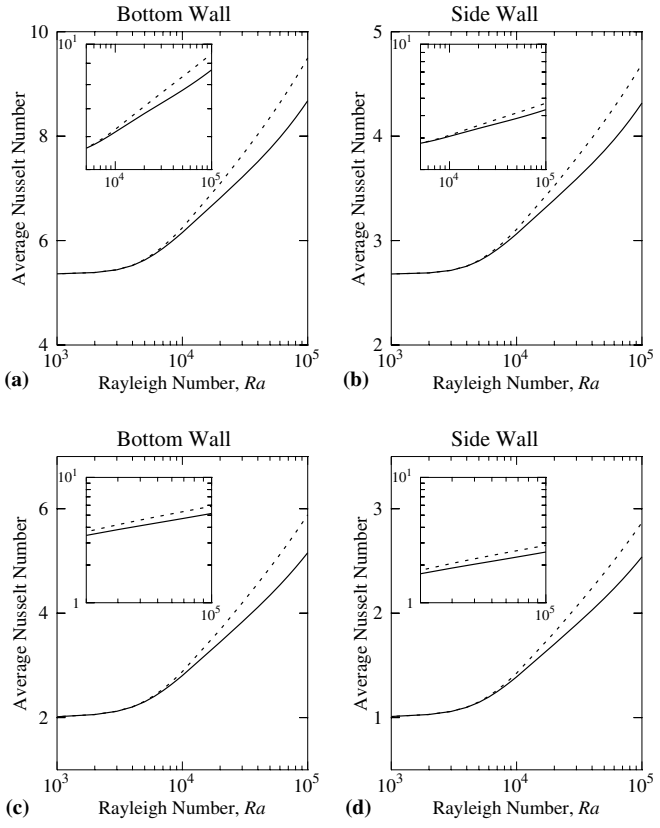

Fig. 10. Variation of average Nusselt number with Rayleigh number for uniform heating [(a) and (b)] and non-uniform heating [(c) and (d)] with $Pr = 0.7$; (—) and $Pr = 10$; (---). The insets show the log–log plot of average Nusselt number versus Rayleigh number for convection dominant regimes.

6. Conclusions

The prime objective of the current investigation is to study the effect of continuous and discontinuous Dirichlet boundary conditions on the flow and heat transfer characteristics due to natural convection within a square enclosure. The penalty finite element method helps to obtain smooth solutions in terms of stream functions and isotherm contours for wide ranges of Pr and Ra with uniform and non-uniform heating of the bottom wall. It has been demonstrated that the formation of boundary layers for both the heating cases occurs. It is also observed that thermal boundary layer develops over approximately 80% of the cavity for uniform heating whereas the boundary layer is approximately 60% for non-uniform heating when $Ra = 10^3$. The heat transfer rate is very high at the edges of the bottom wall and decreases to a minimum value at the center due to uniform heating which is in contrast with the lower heat transfer rate at the edges due to non-uniform heating for $Ra = 10^3$. The conduction dominant heat transfer modes occurs at $Ra \leqslant 5 \times 10^3$ during uniform heating of bottom wall whereas it occurs at $Ra \leqslant 2 \times 10^4$ for non-uniform heating.

At the onset of convection dominant mode, the temperature contour lines get compressed toward the side walls and they tend to get deformed towards the upward direction. During $Ra = 10^5$, the thermal boundary layer develops near the bottom and side walls and the central regime near the top surface has least temperature gradient for both uniform and non-uniform heating. The local Nusselt numbers at the bottom and side walls represent various interesting heating features. The local Nusselt number at the bottom wall is least at the center for uniform heating and there are two minimum heat transfer zones at the

center and the corner points for non-uniform heating. The non-uniform heating exhibits greater heat transfer rates at the center of the bottom wall than that with uniform heating for all Rayleigh numbers. The local Nusselt number at the side wall is found to decrease with distance for conduction dominant heat transfer whereas due to highly dense contour lines near the top portion of the side wall, the local Nusselt number is found to increase for both uniform and non-uniform heating cases. The average Nusselt number indicates overall lower heat transfer rates for non-uniform heating. The average Nusselt number is found to follow a power law variation with Rayleigh number for convection dominant regimes.

References

[1] S. Ostrach, Natural convection in enclosuresAdvances in Heat Transfer, vol. VIII, Academic press, New York, 1972, pp. 161–227.

[2] S. Ostrach, Low-gravity fluid flows, Ann. Rev. Fluid Mech. 14 (1982) 313–345.

[3] S. Ostrach, Natural convection in enclosures, ASME Trans. J. Heat Transfer 110 (1988) 1175–1190.

[4] B. Gebhart, Buoyancy induced fluid motions characteristics of applications in technology: The 1978 Freeman Scholar Lecture, ASME Trans. J. Fluids Eng. 101 (1979) 5–28.

[5] C.J. Hoogendoorn, Natural convection in enclosures, Proc. Eighth Int. Heat Transfer Conf., vol. I, Hemisphere Publishing Corp., San Francisco, 1986, pp. 111–120.

[6] J. Patterson, J. Imberger, Unsteady natural convection in a rectangular cavity, J. Fluid Mech. 100 (1980) 65–86.

[7] V.F. Nicolette, K.T. Yang, J.R. Lloyd, Transient cooling by natural convection in a two-dimensional square enclosure, Int. J. Heat Mass Transfer 28 (1985) 1721–1732.

[8] J.D. Hall, A. Bejan, J.B. Chaddock, Transient natural convection in a rectangular enclosure with one heated side wall, Int. J. Heat Fluid Flow 9 (1988) 396–404.

[9] J.M. Hyun, J.W. Lee, Numerical solutions of transient natural convection in a square cavity with different sidewall temperature, Int. J. Heat Fluid Flow 10 (1989) 146–151.

[10] T. Fusegi, J.M. Hyun, K. Kuwahara, Natural convection in a differentially heated square cavity with internal heat generation, Numer. Heat Transfer Part A 21 (1992) 215–229.

[11] J.L. Lage, A. Bejan, The Ra - Pr domain of laminar natural convection in an enclosure heated from the sider, Numer. Heat Transfer Part A 19 (1991) 21–41.

[12] J.L. Lage, A. Bejan, The resonance of natural convection in an enclosure heated periodically from the side, Int. J. Heat Mass Transfer 36 (1993) 2027–2038.

[13] C. Xia, J.Y. Murthy, Buoyancy-driven flow transitions in deep cavities heated from below, ASME Trans. J. Heat Transfer 124 (2002) 650–659.

[14] M. November, M.W. Nansteel, Natural convection in rectangular enclosures from below and cooled along one side, Int. J. Heat Mass Transfer 30 (1987) 2433–2440.

[15] A. Valencia, R.L. Frederick, Heat transfer in square cavities with partially active vertically walls, Int. J. Heat Mass Transfer 32 (1989) 1567–1574.

[16] M.M. Ganzarolli, L.F. Milanez, Natural convection in rectangular enclosures heated from below and symmetrically cooled from the sides, Int. J. Heat Mass Transfer 38 (1995) 1063–1073.

[17] O. Aydin, A. Unal, T. Ayhan, Natural convection in rectangular enclosures heated from one side and cooled from the ceiling, Int. J. Heat Mass Transfer 5 (1999) 2345–2355.

[18] A.T. Kirkpatrick, M. Bohn, An experimental investigation of mixed cavity natural convection in the high Rayleigh number regime, Int. J. Heat Mass Transfer 29 (1986) 69–82.

[19] M. Corcione, Effects of the thermal boundary conditions at the sidewalls upon natural convection in rectangular enclosures heated from below and cooled from above, Int. J. Therm. Sci. 42 (2003) 199–208.

[20] W.J. Minkowycz, E.M. Sparrow, G.E. Schneider, R.H. Fletcher, Handbook of Numerical Heat Transfer, Wiley, New York, 1988.

[21] T. Basak, K.G. Ayappa, Influence of internal convection during microwave thawing of cylinders, AIChE J. 47 (2001) 835–850.

[22] J.N. Reddy, An introduction to the finite element method, McGraw-Hill, New York, 1993.

[23] G.K. Batchelor, An introduction to fluid dynamics, Cambridge University Press, 1993.

[24] G.D. Mallinson, G.D. Vahl Davis, Three-dimensional natural convection in a box: a numerical study, J. Fluid Mech. 83 (1977) 1–31.